



Octamethylcyclotetrasiloxane-Based, Low-Permittivity Organosilicate Coatings

Composition, Structure, and Polarizability

Yubo Lin,^{a,*} Ting Y. Tsui,^b and Joost J. Vlassak^{a,z}

^aDivision of Engineering and Applied Sciences, Harvard University, Cambridge, Massachusetts 02138, USA

^bTexas Instruments, Incorporated, Silicon Technology Development, Dallas, Texas 75243, USA

Organosilicate glass (OSG) coatings with a range of compositions have been deposited using O₂, He, and octamethylcyclotetrasiloxane as a precursor in a plasma-enhanced chemical vapor deposition process. Rutherford backscattering spectrometry and forward recoil spectrometry were used to determine the composition of the coatings. The measurements show that addition of carbon and hydrogen lowers the density of the coatings, effectively reducing the concentration of the polarizing species. The dielectric constant is further lowered by a reduction of the ionic and orientation polarizabilities. Fourier transform infrared measurements show that as more C and H are incorporated, the siloxane network is more frequently interrupted by terminal methyl (CH₃-) and H groups. Based on the experimental results a quantitative model for the OSG structure is proposed and the inverse infrared absorption cross sections of various absorption bands are determined, some of which for the first time. The structural model also makes it possible to calculate the average electronic polarizability of the various bond configurations in the OSG. © 2006 The Electrochemical Society. [DOI: 10.1149/1.2202120] All rights reserved.

Manuscript submitted October 24, 2005; revised manuscript received January 20, 2006. Available electronically May 19, 2006.

Organosilicate glass (OSG) coatings, often fabricated by means of plasma-enhanced chemical vapor deposition (PECVD) processes using siloxane precursors, are receiving growing attention due to their application in the microelectronic,^{1,2} optical, biomedical,³⁻⁵ and environmental areas. Dense OSG coatings with dielectric constants as low as 2.8 have been successfully integrated into high-performance integrated circuits thanks to their excellent dielectric properties and their compatibility with state-of-the-art process technology. Furthermore, it has been demonstrated that porous OSG coatings can be grown with relative dielectric constants smaller than 2.1,⁶ ensuring that PECVD OSG coatings will be used in future generations of integrated circuits.

PECVD OSG typically consists of an amorphous SiO₂-like network in which some of the bridging oxygen atoms are replaced by organic groups such as CH₃, CH₂, and H. They differ from spin-on dielectrics, which are usually based on methyl silsesquioxane or hydrogen silsesquioxane^{2,7} in that they have a much more diversified bonding structure.⁸ This diversified bonding structure arises as a result of the energetic nature of the PECVD process. In order to gain better insight into the properties of OSG coatings, it is critical to have a good understanding of the structure of the OSG films. Thus far, composition analysis of these coatings has been rather incomplete, especially with respect to the hydrogen content of the coatings. Most surface characterization techniques are not sensitive to light elements and are incapable of hydrogen detection. Rutherford backscattering spectrometry (RBS) is routinely used to measure the composition depth profile of thin films,⁹ but detection of light elements such as C is limited as a result of low sensitivity. In this article, a novel RBS specimen preparation technique is employed to enhance the detection of light elements by decreasing the background signal. Forward recoil spectrometry (FRES, also called elastic recoil detection), is used for hydrogen profiling.^{10,11}

First we present the results of a systematic study of a series of PECVD OSG coatings using RBS, FRES, and Fourier transform infrared (FTIR) spectroscopy. The effect of the deposition process on the structure of the coatings is quantified and linked to their dielectric properties. The mechanical properties and the fracture behavior of the coatings will be discussed in another paper. Then, a quantitative model of the OSG structure is presented that allows extraction of the inverse infrared absorption cross sections of the various functional groups. These cross sections can be used to ana-

lyze the FTIR spectra of other organosilicate coatings quantitatively, without the need for an elaborate characterization of the composition. The model also enables calculation of the electronic polarizabilities of the various bond configurations in the OSG coatings.

Experimental

OSG films were deposited on 200 mm silicon (100) wafers using an industrial PECVD reactor and octamethylcyclotetrasiloxane (OMCTS) as a precursor. Helium and oxygen served as carrier and oxidizer gas, respectively. The composition of the films was varied by changing the OMCTS flow rate. The indices of refraction of the OSG coatings were measured using a V-VASE spectroscopic ellipsometer from J.A. Woollam Co., Inc. The films were scanned over a range of wavelengths from 3000 to 10,000 Å at three different angles of incidence (65, 70, and 75°). The optical properties and thickness of the films were determined by fitting the experimental data using the Cauchy model. The density of the films was measured gravimetrically; the mass of a set of samples was measured using a high-accuracy scale (resolution = 2 μg) before and after stripping the OSG coatings in hydrofluoric acid. The relative dielectric constant was measured using a KLA Quantox XP metrology system.

The atomic concentrations of Si, O, and C were determined by RBS and the H concentration by means of FRES. In order to improve the signal-to-noise ratio of the C signal in the RBS measurements, we used freestanding OSG membranes to eliminate the background signal from the Si substrate. These membranes were fabricated by first depositing 80 nm SiN_x/500 nm OSG/30 nm SiN_x film stacks on Si wafers. SiN_x/OSG/SiN_x membranes were made by opening windows in the silicon substrates using micromachining techniques.^{10,12} The SiN_x capping layers protect the OSG during the micromachining process and prevent the absorption of moisture. A very thin layer of Cu (~5 Å) was sputter-coated onto the specimens immediately prior to the RBS measurements. The Cu was used to reduce charging of the samples and served as an internal reference for calibration of the channel-energy correlations. The samples were irradiated with a 2 MeV 4 He⁺ beam for a total charge of 5 μC. No adverse effect of the radiation on the spectra was observed. The compositions of the films were determined by fitting the experimental spectra with simulated spectra for a SiN_x/OSG/SiN_x film stack obtained using the software package RUMP.^{13,14} The film thicknesses were measured independently using ellipsometry and used as input parameters in the simulation. A typical spectrum and the corresponding simulation for a SiN_x/OSG/SiN_x trilayer are shown in Fig. 1. The stopping powers in the simulations were calculated from

* Electrochemical Society Student Member.

^z E-mail: vlassak@esag.harvard.edu

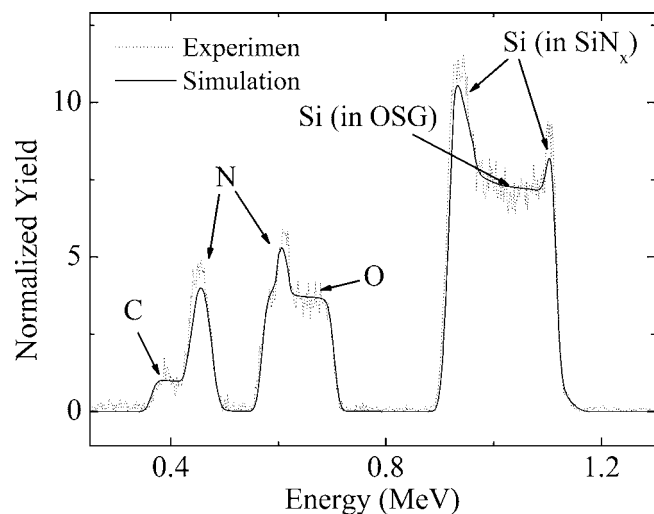


Figure 1. A typical RBS spectrum for a $\text{SiN}_x/\text{OSG}/\text{SiN}_x$ trilayer membrane; the dotted line represents the experimental spectrum while the solid line shows the corresponding simulated spectrum.

the gravimetric film densities; the atomic concentrations of Si, O, and C were derived from the film compositions and gravimetric densities.

For the FRES measurements, a 3 MeV 4He^{2+} beam was configured to bombard the samples at a glancing angle of 15° . Forward-recoiled hydrogen ions were counted by a solid-state detector at 15° from the sample surface, resulting in a scattering angle of 30° . An $11.5\ \mu\text{m}$ thick Mylar foil was placed in front of the detector to block out scattered species other than H. For calibration purposes, a hydrogen-implanted silicon (100) wafer was irradiated under the same conditions and the implanted dose was used as a reference for calculating the H concentration in the OSG films. During irradiation, substantial hydrogen loss from the OSG coatings was observed. Figure 2 shows that this loss becomes increasingly severe with increasing beam dose. Without correction, the H concentration would be underestimated by as much as 30% at $15\ \mu\text{C}$. The H loss was corrected for by extrapolating the He beam charge to zero. By contrast, the H-implanted silicon standard was stable under radiation at a current of 12.5 nA. The FRES results were analyzed using the formalism given by Doyle and Brice.¹⁵ A surface approximation approach was used to calculate the H concentration in the films. In

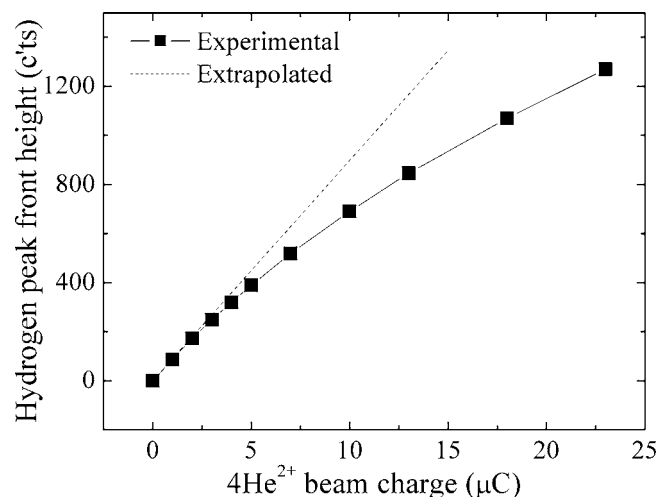


Figure 2. Hydrogen loss during FRES experiment. The dashed line represents the tangent at $0\ \mu\text{C}$ beam charge.

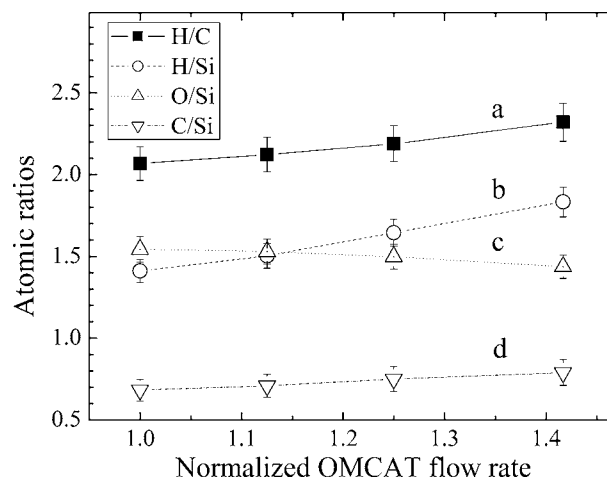


Figure 3. Atomic concentration ratios vs OMCTS flow rate: (a) H/C, (b) H/Si, (c) O/Si, and (d) C/Si.

order to calculate the stopping powers, film densities were computed iteratively using the Si, C, and O densities from the RBS analysis and the H density from the FRES measurements. Non-Rutherford H scattering cross sections measured by Baglin¹⁶ were used in the analysis.

The structure of the OSG coatings was investigated with FTIR spectroscopy. The measurements were made in transmission mode using a Nicolet NEXUS 670 spectrometer equipped with an MCT-A detector and a KBr beam splitter. The infrared beam was incident on the back side of the Si substrate at an angle of 47° to the normal of the sample surface to reduce interference and reflectivity. Before recording each spectrum, the specimen chamber was purged with nitrogen gas for 15 min to reduce interference from ambient moisture and CO_2 . All spectra were collected at a resolution of $2\ \text{cm}^{-1}$. A background spectrum was obtained under the same condition using a blank silicon substrate. The transmittance of the samples was recorded from 4000 to $500\ \text{cm}^{-1}$; the absorbance was determined from the transmittance using

$$A = -\log_{10} T \quad [1]$$

where A and T are absorbance and transmittance, respectively. All spectra were normalized to a film thickness of 1500 nm according to the Beer-Lambert law. Gaussian multipeak fitting was used to analyze overlapping absorption bands allowing peak position, amplitude, and width of each Gaussian to float freely.

Results

Composition and density.— The composition of the OSG coatings is shown in Fig. 3 as a function of OMCTS flow rate. Both the C and H contents increase, while the O content decreases with increasing precursor flow rate. This observation implies that the degree of oxidation of the film decreases with increasing precursor amount. Compared to the precursor itself, $(\text{SiOC}_2\text{H}_6)_4$, the O content of the OSG films is approximately 50% higher, while the C and H contents are considerably smaller. It should be noted that the H/C atomic ratio is smaller than 2.5 for all films (Fig. 3). This low ratio suggests that in addition to CH_3 there must be a significant fraction of CH_2 groups in the OSG; this is indeed confirmed by the FTIR measurements. It may even be possible that a small amount of C does not bond directly to H. These C atoms may be present in the form of silicon carbide or oxycarbide as is observed after pyrolysis of polysiloxane polymers,¹⁷ although there is no direct evidence for the presence of such groups. As shown in Table I, the density of OSG decreases with increasing OMCTS flow rate. Clearly, addition of C and H increases the number of organic groups in the siloxane network and opens up the OSG network structure.

Table I. Properties of OSG films and amorphous silica.

Film	OSG-1	OSG-2	OSG-3	OSG-4	<i>a</i> -Silica
Normalized OMCTS flow rate (f/f_0)	1.00	1.13	1.25	1.42	
Density (g/cm^3)	1.525	1.475	1.446	1.403	2.25
Refractive index at 633 nm	1.450	1.444	1.440	1.438	1.46
Relative dielectric constant at 1 MHz	3.33	3.22	3.16	3.08	4.0
$\frac{(k-1)}{(k+2)} \cdot \frac{M}{N_0\rho} \cdot \frac{3}{4\pi} (\text{\AA}^3)$	7.29	7.17	7.12	6.99	5.29
$\frac{(n^2-1)}{(n^2+2)} \cdot \frac{M}{N_0\rho} \cdot \frac{3}{4\pi} (\text{\AA}^3)$	4.485	4.483	4.482	4.480	2.90

Electrical and optical properties.—The relative dielectric constants of the OSG coatings are tabulated in Table I. The value of the dielectric constant drops from 3.33 to 3.08 as the OMCTS flow rate is increased. According to the Debye equation, the relative dielectric constant, k , of a material is given by

$$\frac{k-1}{k+2} = \frac{4\pi N}{3} \left(\alpha_e + \alpha_d + \frac{\mu^2}{3kT} \right) \quad [2]$$

where N is the number density of the polarizing species, α_e the electronic polarization, α_d the ionic or distortion polarization, and μ the polarization due to orientation of permanent dipoles. The density of dipoles can be written as $N = N_0\rho/M$, where N_0 is the Avogadro constant, ρ the mass density, and M the formula weight of the dipoles. It then follows that

$$\frac{k-1}{k+2} \cdot \frac{M}{N_0\rho} \cdot \frac{3}{4\pi} = \alpha_e + \alpha_d + \frac{\mu^2}{3kT} \quad [3]$$

The sum of the quantities on the right side now represents the average polarizability of one formula unit of OSG. Thus, if the change of the dielectric constant is due to a decrease in the density of the polarizing species, the left side of Eq. 3 should remain constant. As illustrated in Table I, this is not the case. Figure 4 shows a graph of the OSG dipole density and the corresponding average molecular polarizability. Clearly, the reduction in dielectric permittivity with increasing C content is a consequence of a decrease in both the density of the polarizing species and the average molecular polarizability, at least for the range of C concentrations considered here. The results in Table I further show that OSG has a higher polarizability per formula unit than amorphous silica. This observation implies that OSG has a lower dielectric constant than silica because of its much lower density, rather than a lower intrinsic polarizability.

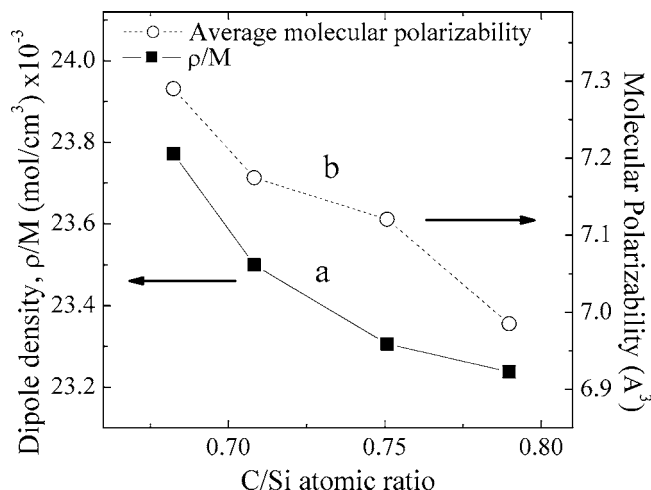


Figure 4. (a) Dipole density and (b) the average polarizability per formula unit of OSG as a function of carbon content.

Table I lists the refractive indices, n , of the coatings at a wavelength of 633 nm, along with the index of refraction of fused silica. All OSG films have a smaller refractive index than silica. It follows from Maxwell's equations that the square of the refractive index is equal to the relative dielectric constant.^{2,18} Because only electronic polarization plays a role at optical frequencies, the index of refraction can be used to assess the contribution of the electronic polarization to the dielectric constant of OSG. From Eq. 3, one finds

$$\alpha_e = \frac{3}{4\pi} \cdot \frac{M}{N_0\rho} \cdot \frac{n^2-1}{n^2+2} \quad [4]$$

According to Eq. 4, electronic polarizability accounts for approximately two-thirds of the total polarization. Furthermore, the electronic polarization per formula unit remains nearly constant when the OMCTS flow rate is increased (Table I). Consequently, the decrease in the polarizability with OMCTS flow rate is caused by a decrease in the ionic and orientation polarizability. Because ionic and orientation polarization are sensitive to the precise bonding configuration, the variation of the dielectric constant suggests that there are subtle changes in the network structure of the OSG coatings as the flow rate is increased. Indeed, as is seen in the next section, films deposited at higher OMCTS flow rates contain more Si-CH₃ and Si-CH₂ bonds, which reduce ionic and orientation polarization.

FTIR analysis.—A typical FTIR absorbance spectrum for the OSG coatings is depicted in Fig. 5. The spectrum shows several broad absorption bands representing the diversified film structure that results from the plasma polymerization process. Infrared spectra for OMCTS monomers or spin-on films usually show narrower and sharper absorption bands,^{7,19} as one would expect for materials with a well-defined structure. Detailed peak assignments are listed in Table II.

The broad absorption band from 1200 to 950 cm⁻¹ belongs to the Si-O-Si asymmetric stretching mode, typical for a siloxane net-

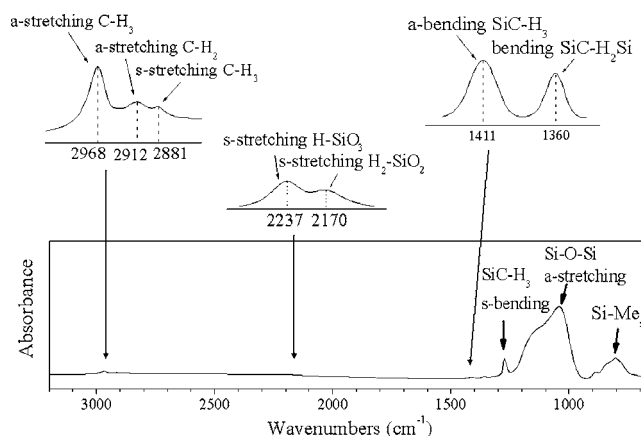
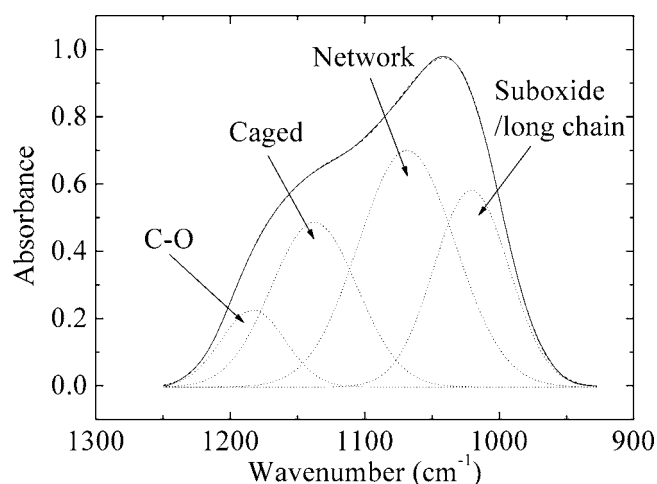


Figure 5. Representative FTIR spectrum of OSG films with major absorption bands labeled.

Table II. Infrared band assignments of OSG films. ν = stretching, δ = bending, ρ = rocking, a = asymmetric, s = symmetric vibrations, and Me = CH₃.

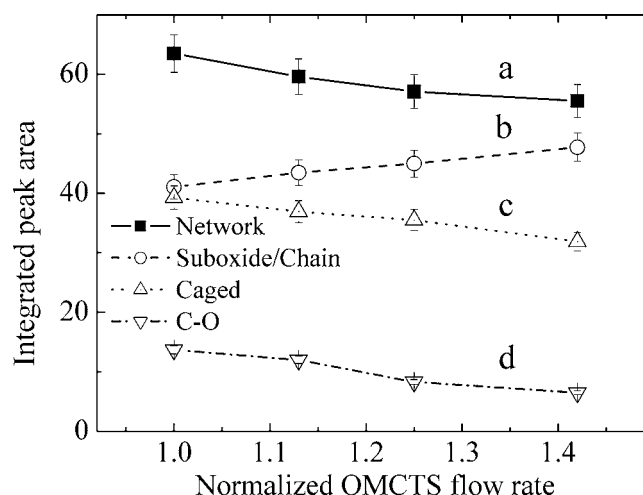
Wavenumber (cm ⁻¹)				Mode	Comment	Reference
OSG-1	OSG-2	OSG-3	OSG-4			
C-H _x (n = 2,3) related modes						
2969	2968	2968	2968	ν^a C-H ₃	sp^3 CH ₃	18, 19, 25, and 36
2916	2915	2915	2914	ν^a C-H ₂	sp^3 CH ₂	18, 19, 25, and 36
2880	2879	2879	2879	ν^s C-H ₃	sp^3 CH ₃	18, 19, 25, and 36
2851	2851	2851	2851	ν^s C-H ₂	sp^3 CH ₂	18, 19, 25, and 36
Si-CH ₂ related modes						
1360	1360	1360	1360	δ C-H ₂	Si-CH ₂ -Si	18 and 19
Si-CH ₃ related modes						
1412	1412	1412	1412	δ^a C-H ₃	Si-(CH ₃) _x	18, 19, and 26
1274	1273	1273	1273	ρ C-H ₃	Si-(CH ₃) _x	18, 19, 23, 26, and 28
840	840	840	840	ν Si-C, ρ CH ₃	Si-(CH ₃) ₃	18, 19, 23, 25, and 26
803	804	804	804	ν Si-C, ρ CH ₃	Si-(CH ₃) ₂	8, 18, 19, 23, 25, and 26
775	777	777	778	ν Si-C, ρ CH ₃	Si-(CH ₃) ₁	18, 19, 23, 25, and 26
745	741	736	731	ν^a Si-C	Si-C	25 and 32-34
				ν Si-O	Si-O-Si	19, 22, 31, and 35
Si-H related modes						
2239	2238	2236	2235	ν Si-H	H-SiO ₃	8, 19, 22, 25, and 30
2176	2175	2173	2172	ν Si H ₂	H ₂ -SiO ₂	8, 19, 25, and 30
890	891	892	893	δ H-Si-O	H-SiO ₃	19, 22, 24, 30, and 31
Si-O related modes						
1183	1181	1182	1177	ν^a Si-O-C	Si-O-CH ₃	21, 25, and 29
1137	1138	1143	1145	ν^a Si-O	CH ₃ Si-O ₃ cage	19, 22, and 28
1069	1072	1077	1083	ν^a Si-O	SiO ₂ network, OMCTS ring	19, 21, and 22, Monomer ¹⁸
1020	1022	1024	1026	ν^a Si-O	Si-O suboxide, long chain	8, 19, 20, and 23-27
1110- 1075				ν C-O	Si-O-C	19, 21, 23, and 25

work or chain. This band consists of several overlapping peaks that correspond to Si-O-Si bonds in different configurations. Four bond types were identified as shown in Fig. 6. The peak in the center, near 1075 cm⁻¹, represents a typical SiO₂-like network where each Si atom is bound to four O atoms.²⁰⁻²² Since the Si-O-Si asymmetric stretching mode in the OMCTS monomer also occurs at this frequency,¹⁸ this peak may also include contribution from any retained OMCTS rings in the film. The peak at 1023 cm⁻¹ is attributed to various suboxidized states of the siloxane network,^{8,11,20,23-27} such as long polymeric chains, ring structures, or more random forms. The shoulder at 1141 cm⁻¹ usually indicates a cage structure^{19,22,28} similar to that in silsesquioxane polymers. The weak peak at

**Figure 6.** Deconvolution of the Si-O-Si asymmetric stretching band.

1180 cm⁻¹ is attributed to C-O stretching in some methoxysiloxane species.^{21,25} This peak was also observed by Chiang et al. in OSG films deposited with OMCTS precursor.²⁹ The peak areas of these components are plotted as a function of OMCTS flow rate in Fig. 7. The figure clearly shows that the fractions of the SiO₂-like network and the caged structure decrease while the amount of suboxide increases with OMCTS flow rate. The peak positions in Table II show a blue shift for the Si-O vibration modes with increasing OMCTS flow rate. This may be caused by an increase in the Si-O-Si bond angle as the OSG density decreases.³⁰

The peak at 1273 cm⁻¹ is attributed to the Si-(CH₃)_x (x = 1, 2,

**Figure 7.** FTIR peak area for different Si-O bond structures as a function of OMCTS flow rate: (a) network, (b) suboxide/chain, (c) caged, and (d) C-O.

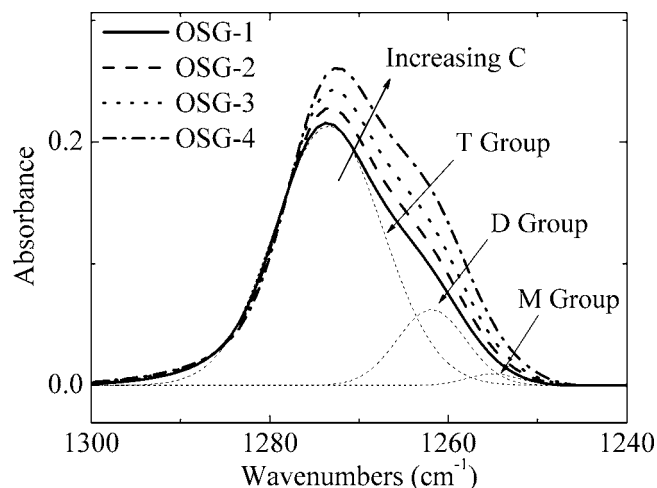


Figure 8. The SiC-H₃ symmetrical bending band. The thin dashed lines show the deconvoluted peaks for the T, D, and M components in OSG-1.

or 3) rocking mode. It is one of the characteristic peaks in the infrared spectrum of a methylpolysiloxane film. Figure 8 shows a detailed view of this band. With increasing OMCTS flow rate, i.e., increasing C content, the peak becomes stronger due to incorporation of additional methyl groups; it shifts to a lower frequency (red shift) and develops a shoulder. This evolution is related to the bonding state of the silicon atom connected to the methyl groups and results from an increased number of D- and M-groups relative to T-groups.^{26,28} In this nomenclature, a T-group corresponds to O₃Si-CH₃, where three oxygen atoms and one organic group (methyl group in the present case) are connected to a single silicon atom. The D- and M-groups represent O₂Si-(CH₃)₂ and OSi-(CH₃)₃, respectively. The shoulder at lower frequency indicates an increased number of D- and M-groups in the film. The peak can be decomposed into its three constituents using Gaussian peak fitting. The results are listed in Table III. The peak area for each of the three groups, i.e., the absolute number of methyl groups in each configuration, rises with increasing C content. As expected, the fraction of methyl groups in a D or M configuration increases, while the fraction of the T-groups decreases as more methyl groups are incorporated into the coatings. The relative amounts of these configurations are important for the network structure of the OSG: T-groups have three bridging atoms and can thus be part of a caged structure or a network, D-groups are nodes in a linear chain, and M-groups terminate a chain or network. Consequently, one would expect mechanical properties such as the stiffness, hardness, or fracture toughness of the OSG coatings to depend sensitively on the precise bonding configuration of the methyl groups.

The broad band between 900 and 700 cm⁻¹ (Fig. 5) consists of overlapping vibration modes from various bond structures. As illustrated in Fig. 9, at least five peaks are necessary to get a good deconvolution of the band. The three sharp peaks at 840, 804, and 777 cm⁻¹ can be assigned to coupling of the Si-C stretching and the CH₃ rocking modes in the Si-(CH₃)_x (x = 1-3)

Table III. Deconvolution of the infrared Si(C-H₃)_x symmetric bending absorption band.

Film	OMCTS flow rate	T (1273 cm ⁻¹)		D (1262 cm ⁻¹)		M (1254 cm ⁻¹)	
		Area	%	Area	%	Area	%
OSG-1	1.00	3.23	82.9	0.59	15.3	0.07	1.8
OSG-2	1.13	3.43	81.4	0.68	16.0	0.11	2.6
OSG-3	1.25	3.68	80.4	0.75	16.4	0.15	3.2
OSG-4	1.42	3.96	78.5	0.86	17.1	0.22	4.4

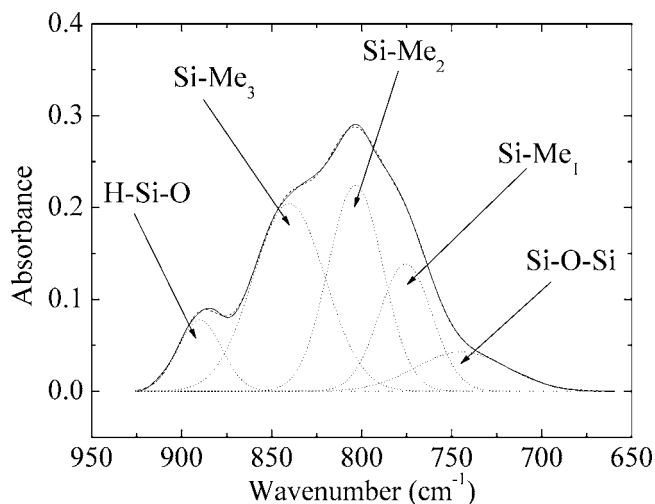


Figure 9. Deconvoluted peaks for the infrared absorption band from 925 to 650 cm⁻¹.

structure.^{8,18,19,23,25,26} The shoulder at 890 cm⁻¹ may be assigned to Si-O stretching^{19,22,24,30,31} in either the HSiO₃ or the SiOH configuration. In the present case, the assignment to HSiO₃ is the more likely because there is no OH absorption band at 3500 cm⁻¹. The weak band at 745 cm⁻¹ may be attributed to the Si-C stretching mode in a carbide structure^{25,32-34} or the symmetric stretching mode of Si-O-Si bonds.^{19,22,31,35}

The infrared spectra of the OSG coatings also exhibit a number of fine structures that are shown more clearly in the inserts in Fig. 5. The C-H_x (x = 2 or 3) stretching band from 2990 to 2840 cm⁻¹ consists of four different vibration modes: *v*^aC-H₃, *v*^aC-H₂, *v*^sC-H₃, and *v*^sC-H₂.^{18,19,25,36} Figure 10 shows an expanded view of this part of the spectrum along with the Gaussian fits corresponding to each of the vibration modes. The *v*^aC-H₂ and *v*^sC-H₂ peaks are direct evidence of the presence of methylene groups in the OSG network. Methylene groups form bonds to two Si atoms and perform a cross-linking function in the OSG network; by contrast, methyl groups replace a bridging oxygen atom with a terminal group and disrupt the network. Thus, the number of methylene relative to methyl groups in the structure of the films is critical to the integrity of the network structure. As the C content of the OSG films increases, the *v*^aC-H₂/C-H₃ peak area ratio decreases (see Table IV), indicat-

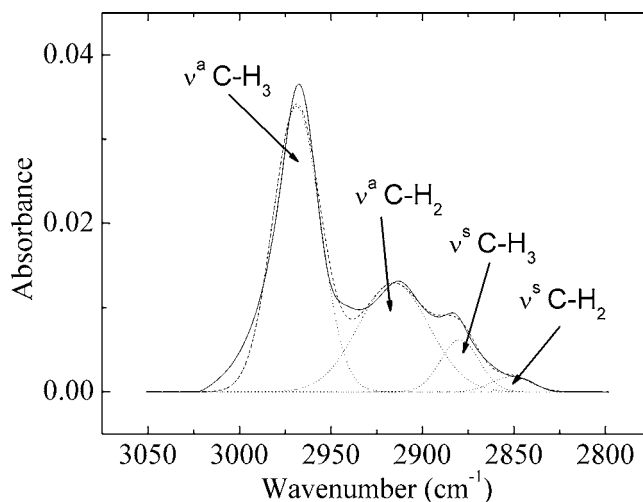


Figure 10. Peaks in the C-H_{x=2,3} stretching band from 2990 to 2840 cm⁻¹. The solid line is the experimental spectrum.

Table IV. Infrared-peak-area ratios of functional groups in OSG films.

Peak-area ratios	OSG-1	OSG-2	OSG-3	OSG-4
ν^a C–H ₂ /C–H ₃	0.565	0.547	0.509	0.448
ν H–Si/H ₂ –Si	1.007	0.947	0.887	0.786
ρ C–H ₃ / ν^a Si–O	0.0253	0.0284	0.0324	0.0370

ing a shift from methylene to methyl groups and a degradation of the network structure of the OSG. This observation is further confirmed by the C–H₂ and C–H₃ bending modes between 1300 and 1500 cm⁻¹: the C–H₃ asymmetric bending mode from Si(CH₃)_x at 1411 cm⁻¹ increases with C content, while the C–H₂ bending mode from SiCH₂Si at 1360 cm⁻¹ decreases.

Finally, information obtained from the H–Si stretching band from 2300 to 2110 cm⁻¹ leads to a similar conclusion. This band consists of two peaks: a peak at 2237 cm⁻¹ attributed to the H–SiO₃ structure and a peak at 2174 cm⁻¹ that arises because of H₂SiO₂.^{8,19,25,30} H–SiO₃ can be regarded as part of a caged structure or suboxide network, while H₂SiO₂ forms a linear chain. As the C content of the films increases, the H–SiO₃/H₂SiO₂ peak area ratio, which is another indication of the degree of cross-linking in the siloxane network, decreases (see Table IV). The H–Si stretching band is very weak, suggesting that there are few H–Si bonds in the OSG. This is not surprising given that the precursor does not contain any Si–H bonds and that the Si–H bond is weaker than most of the other bonds in the network.

Analysis and Discussion

With structural information provided by the FTIR spectra and atomic concentrations determined from RBS and FRES, a quantitative analysis of the OSG is performed. In this analysis, the structure of the OSG is described in terms of building blocks, each one of which corresponds to a functional group identified in the FTIR spectra and represents part of the OSG network. The analysis is briefly discussed here; more details and calculations are reported in the Appendix.

Our analysis relies on the FTIR spectra to identify the functional groups present in the OSG coatings, including Si–O–Si, –CH₃, –CH₂–, and –H. Based on these groups, five building blocks are defined as illustrated in Fig. 11. The corresponding formula units are SiO₂, (CH₃)_{2m}SiO_{2–m}, Si(CH₂)_{0.5}O_{1.5}, Si(CH₂)O, and H_{2p}SiO_{2–p}. Note that these formulas reflect the exact proportion of atoms associated with each functional group. For example, the T-group, represented as O₃Si–CH₃ in Table II, is written as (CH₃)SiO_{1.5}, because each of the three O atoms is shared with another Si atom. Thus, SiO₂ represents the part of the network that is just like silica; (CH₃)_{2m}SiO_{2–m} is a combination of the T, D, and M groups; H_{2p}SiO_{2–p} combines the mono- and bisubstituted H–Si bonds; Si(CH₂)_{0.5}O_{1.5} and Si(CH₂)O are two different CH₂-related configurations that cross-link the network. The value of *m* in

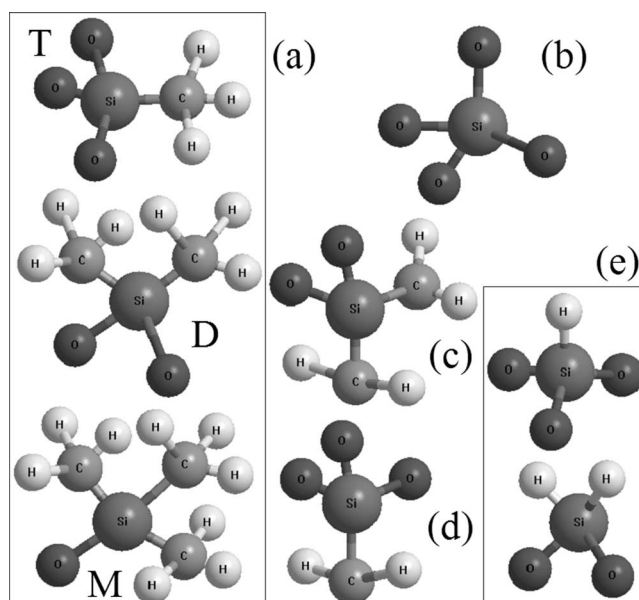


Figure 11. Building blocks identified in the OSG network, including (a) (CH₃)_{2m}SiO_{2–m}, (b) SiO₂, (c) SiCH₂O, (d) Si(CH₂)_{0.5}O_{1.5}, and (e) H_{2p}SiO_{2–p}.

(CH₃)_{2m}SiO_{2–m} is determined by the relative number of T, D, and M groups and can be estimated from the relative peak intensities in the FTIR spectrum (See Table III or the absorption peaks in Fig. 8); similarly, the value of *p* can be determined from the peaks around 2200 cm⁻¹.

The infrared absorption cross sections of the functional groups are not known for OSG-like materials. Thus, it is not possible to determine what fraction of the OSG network is made up of the individual building blocks based on an analysis that relies solely on the FTIR absorption results. A quantitative analysis is feasible in the present case, however, because data is available for a series of OSG samples of different composition. If the absorption cross sections are the same for all the OSG samples, they can be calculated by combining the FTIR results with the composition results of the elemental analysis. Assuming that the absorption cross sections do not vary from sample to sample is justified because of the relatively small differences in composition between the samples and the similarity of their structure as evidenced by the FTIR spectra. Based on the mass balances for each of the atomic species in the OSG and the FTIR absorption data, it is possible to derive a set of equations from which the concentrations of the building blocks can be calculated using a least squares technique. A detailed description of the procedure is given in the Appendix. Once the concentrations are known, the absorption cross sections are readily determined.

Table V. Concentration of the various bond configurations in the OSG films. The two configurations containing a CH₂ group are represented by Si(CH₂)_xO_{2–x}; *x* is listed in the last column.

Film	Bond configuration concentration (10 ²² cm ⁻³)						<i>x</i>
	SiO ₂	(CH ₃) _{2m} SiO _{2–m}	H _{2p} SiO _{2–p}	SiCH ₂ O	Si(CH ₂) _{0.5} O _{1.5}	Si(CH ₂) _x O _{2–x}	
OSG-1	0.38±0.02	0.35 ± 0.02	0.19±0.04	0.13±0.02	0.39 ± 0.03	0.51 ± 0.05	0.62
OSG-2	0.37±0.03	0.36 ± 0.02	0.19±0.04	0.15±0.03	0.34 ± 0.05	0.50 ± 0.07	0.65
OSG-3	0.34±0.03	0.40 ± 0.02	0.19±0.04	0.20±0.03	0.26 ± 0.05	0.46 ± 0.07	0.72
OSG-4	0.28±0.03	0.46 ± 0.03	0.18±0.04	0.26±0.03	0.18 ± 0.05	0.44 ± 0.07	0.79

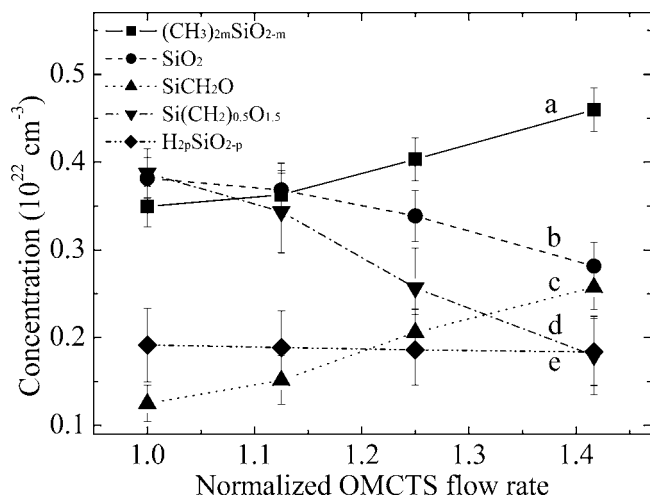


Figure 12. Concentrations of the various bond configurations as a function of OMCTS flow rate: (a) $(\text{CH}_3)_{2m}\text{SiO}_{2-m}$, (b) SiO_2 , (c) SiCH_2O , (d) $\text{Si}(\text{CH}_2)_{0.5}\text{O}_{1.5}$, and (e) $\text{H}_{2p}\text{SiO}_{2-p}$.

In addition to the functional groups identified in the FTIR analysis, the OSG may also contain groups that cannot be detected by FTIR such as silicon carbide or oxycarbide. If the OSG contains a significant fraction of unidentified groups, it is not possible to find a set of concentrations that satisfies the equations. In that case, it may be necessary to use other techniques such as nuclear magnetic resonance or Raman scattering to identify the groups and improve the accuracy of the analysis.

The results of the model are listed in Table V and are shown graphically in Fig. 12. The error bars in the figure were determined from a statistical analysis of the least-squares solution based on the chi square distribution. The errors are relatively small, indicating that the concentration of groups not detected by the FTIR analysis is not significant. Any systematic errors in the composition analysis are of course not reflected in the error bars. We expect the largest systematic error to occur because the H concentration was determined using a different technique than the Si, O, and C concentrations, even though every effort was made to minimize this error. To give an idea of how this error impacts the analysis, a 5% error in the hydrogen content of the OSG would result in an error of at most 10% in the number density of SiO_2 , $(\text{CH}_3)_{2m}\text{SiO}_{2-m}$, $\text{Si}(\text{CH}_2)_{0.5}\text{O}_{1.5}$, and $\text{Si}(\text{CH}_2)\text{O}$, while the concentration of $\text{H}_{2p}\text{SiO}_{2-p}$ could be affected by as much as 40%.

Figure 12 shows that the OSG structure consists mainly of siloxane along with significant fractions of methyl and methylene groups. The SiO_2 fraction of the network decreases with increasing OMCTS flow rate, while the concentration of bonds to methyl groups increases. The concentration of $\text{Si}(\text{CH}_2)_{0.5}\text{O}_{1.5}$ decreases with increasing OMCTS flow rate, while that of $\text{Si}(\text{CH}_2)\text{O}$ increases, possibly as the result of an increase in the $\text{Si}-\text{CH}_2^*$ radical concentration in the plasma.

Since OSG is essentially a SiO_2 network with a fraction of the $\text{Si}-\text{O}$ bonds substituted by $\text{Si}-\text{CH}_3$, $\text{Si}-\text{CH}_2$, and $\text{Si}-\text{H}$ bonds, one would expect the physical properties of the films to correlate with the concentration of these bonds. Figure 13, for example, shows the relative dielectric constant as a function of the $(\text{Si}-\text{CH}_3 + \text{Si}-\text{CH}_2 + \text{Si}-\text{H})/\text{Si}-\text{O}$ bond density ratio. As expected, the dielectric constant decreases with increasing ratio. As pointed out in the Results section, this decrease is the result of both a change of density and a change in the structure of the film. By extrapolating to zero, one finds a relative dielectric constant of 4.04 ± 0.21 , which is close to the value for silica. With the concentration of the various bond configurations known, we are now able to calculate the average electronic polarizability for individual bond configurations. The

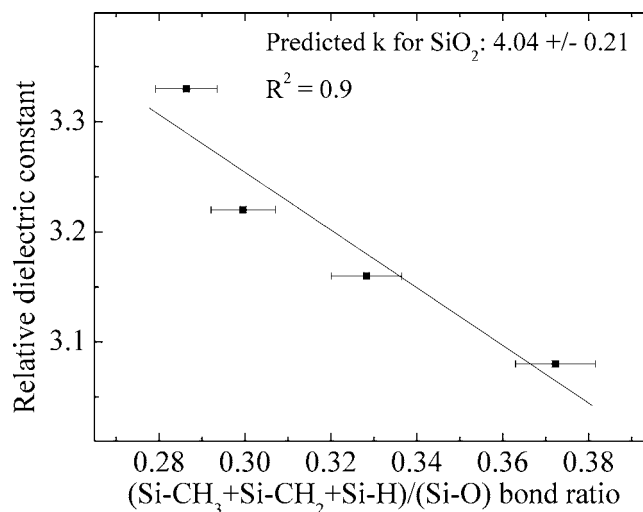


Figure 13. Relative dielectric constant as a function of $(\text{Si}-\text{CH}_3 + \text{Si}-\text{CH}_2 + \text{Si}-\text{H})/\text{Si}-\text{O}$ bond density ratio.

values are tabulated in Table VI. The electronic polarizability of SiO_2 as determined from the model is 2.87 \AA^3 , in close agreement with literature data.^{37,38} The numbers for $(\text{CH}_3)_{2m}\text{SiO}_{2-m}$ and $\text{Si}(\text{CH}_2)_x\text{O}_{2-x}$ are larger than for SiO_2 , because replacing the $\text{Si}-\text{O}$ bond with $\text{Si}-\text{CH}_3$ or $\text{Si}-\text{CH}_2$ bond breaks the $\text{Si } sp^3$ symmetry. This causes a shift in the electron distribution around the Si atom and results in a stronger molecular dipole moment. The lower electronic polarizability of $\text{H}_{2p}\text{SiO}_{2-p}$ may be attributed to the reduced charge of H and/or a change of bond angles.³⁹ It is not possible to calculate accurate ionic or orientation polarizabilities of the bond configurations because those quantities are much more sensitive to the precise bond environment.

The quantitative analysis of the OSG structure makes it possible to calculate the correlation coefficients between the integrated FTIR absorbance and the bond densities. These coefficients allow one to directly calculate bond densities from an FTIR spectrum. According to the Beer-Lambert law, the absorption coefficient α is related to the transmittance by

$$\ln T = -\alpha \cdot d \quad [5]$$

where d is the optical path length, which depends on film thickness and the infrared beam incident angle. Using Eq. 1 and 5, the absorption coefficient can be written in terms of the absorbance

$$\alpha = \ln 10 \frac{A}{d} = 2.3026 \frac{A}{d} \quad [6]$$

Equation 6 is used to determine the absorption coefficients from the FTIR absorbance spectra. The density, Q , of a given functional group can then be calculated from

$$Q = A_s \int \frac{\alpha(\nu)}{\nu} d\nu \quad [7]$$

where A_s is the inverse IR absorption cross section of the group and ν is the vibration frequency of the corresponding absorption band. The inverse IR absorption cross sections of the various functional groups in OSG were calculated and they are listed in Table VII. The

Table VI. Average electronic polarizability of the various bond configurations in the OSG films.

	SiO_2	$(\text{CH}_3)_{2m}\text{SiO}_{2-m}$	$\text{Si}(\text{CH}_2)_x\text{O}_{2-x}$	$\text{H}_{2p}\text{SiO}_{2-p}$
$\alpha_e (\text{\AA}^3)$	2.87	5.47	5.90	2.05

Table VII. Inverse infrared cross sections of absorption bands in OSG films and literature data for these absorption bands in other materials.

Mode	Wavenumber (cm ⁻¹)	Correlation constant (10 ²⁰ cm ⁻²)	
		Model	Literature number
C-H _x stretching	2990–2835	28.6 ± 4.1	10, ⁴⁰ 17 ⁴¹
H _x -Si <i>s</i> -stretching	2265–2145	4.42 ± 1.47	1.72, ⁴² 1.4, ⁴³ 1.7 ⁴⁴
C-H ₃ bending	1412	14.9 ± 2.4	
C-H ₂ bending	1360	23.0 ± 6.6	
C-H ₃ rocking	1273	1.23 ± 0.14	
Si-O <i>a</i> -stretching	1160–1000	0.16 ± 0.03	0.15 ³⁴
H-SiO ₃ bending	890	1.14 ± 0.43	
Coupling of Si-C stretching and CH ₃ rocking	840–777	0.14 ± 0.02	

standard deviations represent the statistical errors derived from a chi square analysis of the model. Given the uncertainty in the H_{2p}SiO_{2-p} concentration, the corresponding inverse cross section should be treated with some suspicion. The inverse cross section for the other groups, however, should be quite accurate. Some inverse cross sections for the same bonds in other materials obtained from the literature are also listed for reference. Values of IR absorption cross sections are typically very sensitive to the bond environment, although cross sections of weak dipoles tend to be more sensitive to bond environment than strong dipoles such as Si-O, because IR absorption reflects the effective charge associated with the bond. As expected, the inverse cross section for Si-O-Si asymmetric stretching from 1160 to 1000 cm⁻¹ is 0.16 ± 0.03 × 10²⁰ cm⁻², in good agreement with the value calculated by Basa³⁴ for quartz. The cross sections for weaker dipoles, such as C-H and Si-H, do not agree quite that well with the literature values. This is to be expected because the literature values were measured for bonds in very different materials. For instance, the values for C-H were measured for hydrogenated silicon carbide in both references,^{40,41} while the values for Si-H were obtained from hydrogenated amorphous silicon.⁴²⁻⁴⁴ The experimental values listed in Table VII are all greater than the corresponding literature values. We attribute this to an inductive effect between neighboring bonds. The inverse cross sections depend sensitively on the effective vibrating charge of the bonds and hence on the bonding environment.²⁶ For example, oxygen is much more electronegative (3.44) than Si (1.9), C (2.55), and H (2.2) and forms a strong dipole with Si, thus reducing the effective charge of any adjacent Si-H bonds. Consequently, the inverse cross section for Si-H is expected to be higher in OSG than in hydrogenated amorphous silicon. Several of the inverse cross sections tabulated in Table VII have been measured for the first time to the best of our knowledge. We expect that these inverse cross sections will be useful for future studies of OSG-like materials.

Conclusions

We have investigated the composition, structure, and dielectric properties of OSG coatings deposited by means of PECVD as a function of the OMCTS precursor flow rate. RBS and FRES analysis show that OSG films incorporate more C and H, and less O, when the OMCTS flow rate is increased relative to the oxygen flow rate. The result is a net decrease in film density and relative dielectric constant. The reduction in the dielectric constant is due to both a decrease in dipole density and molecular polarizability. The lower dielectric constant of OSG as compared to silica is attributed mainly to the much lower density of OSG.

A detailed FTIR analysis reveals that the film becomes less cross-linked when the OMCTS flow rate increases because the siloxane network is more and more interrupted by -CH₃ and -H groups. We propose a quantitative model for the OSG structure based on the functional groups identified using FTIR. The model makes it possible to determine the electronic polarizabilities of the individual bond configurations in OSG and the value obtained for

SiO₂ is in very good agreement with data from the open literature. Furthermore, the inverse IR absorption cross section for Si-O-Si asymmetric stretching derived from the model is in very good agreement with data available in the literature.

Acknowledgments

Financial support from the Division of Engineering and Applied Sciences at Harvard University and the Semiconductor Research Corporation (contract 1292.010) is gratefully acknowledged. The authors also wish to thank S. Martin in DEAS at Harvard University for the use of an FTIR spectrometer, J. Chervinsky at the Cambridge Accelerator for Materials Science for assistance with FRES and RBS experiments, and the management of Silicon Technology Development, Texas Instruments, for in-kind support.

Harvard University assisted in meeting the publication costs of this article.

Appendix: A Structural Model for OSG

In the analysis, OSG is assumed to consist of a number of bond configurations that each contains one Si atom and that serve as building blocks for the structure. The relevant bond configurations are identified in the FTIR absorption spectra of the OSG coatings. The fraction of the OSG structure that consists of each configuration is determined from the FTIR spectra along with the mass balances for each of the atomic species in the OSG coatings. The underlying assumptions are the following:

1. The infrared absorption cross section of a given functional group does not change significantly as the OSG deposition parameters are changed. This assumption is acceptable because the structure of the OSG does not vary much over the range of deposition parameters explored in this study, as evidenced by the FTIR spectra. If the cross sections are independent of the process parameters, it is possible to compare the densities of a given functional group in different films using the corresponding infrared absorption band areas and the inverse infrared absorption cross sections can be treated as unknown parameters to be determined from the analysis.

2. Vibration modes that are very similar and that occur at nearly the same wavenumber have similar infrared absorption cross sections. Examples are the C-H₃ and C-H₂ stretching modes^{40,41} from 2968 to 2915 cm⁻¹, the Si-H and Si-H₂ stretching modes⁴²⁻⁴⁴ from 2237 to 2175 cm⁻¹, the various Si-O-Si *a*-stretching modes³⁴ near 1074 cm⁻¹, and the T, D, and M Si-CH₃ rocking modes near 1273 cm⁻¹. Consequently, the relative amounts of these groups can be determined directly from the integrated areas of the corresponding peaks. The relevant building blocks in the model are written as H_{2p}SiO_{2-p} and (CH₃)_{2m}SiO_{2-m}, where (CH₃)_{2m}SiO_{2-m} is a combination of the T, D, and M groups identified by the peak at 1273 cm⁻¹; H_{2p}SiO_{2-p} combines the mono- and disubstituted H-Si bonds from ~2200 cm⁻¹. The subscripts *p* and *m* are calculated from the corresponding peak area ratios for each set of deposition conditions (listed in Table A-I). This assumption is not essential but reduces the complexity of the analysis by limiting the number of building blocks in the model. It also allows for a comparison of similar groups such as CH₃ and CH₂ in the same film using the corresponding infrared absorption bands.

Table A-I. Parameters *p* and *m* in H_{2p}SiO_{2-p} and (CH₃)_{2m}SiO_{2-m}.

Film	<i>p</i>	<i>m</i>
OSG-1	0.666	0.549
OSG-2	0.664	0.554
OSG-3	0.701	0.558
OSG-4	0.673	0.565

Table A-II. Elemental contribution coefficients a_j^k for each configurational group.

No.	1	2	3	4	5	6
	$H_{2p}SiO_{2-p}$	$Si(CH_2)_{0.5}O_{1.5}$	$Si(CH_2)O$	$(CH_3)_{2m}SiO_{2-m}$	SiO_2	Residual C
Si	1	1	1	1	1	0
O	$2 - p_i$	1.5	1	$2 - m_i$	2	0
C	0	0.5	1	$2m_i$	0	1
H	$2p_i$	1	2	$6m_i$	0	0

3. The analysis relies on the FTIR spectra for identification of the major building blocks present in the OSG coatings. These include SiO_2 , the two combination units mentioned in last section [$(CH_3)_{2m}SiO_{2-m}$ and $H_{2p}SiO_{2-p}$], and two CH_2 -related configurations [$Si(CH_2)_{0.5}O_{1.5}$ and $Si(CH_2)O$]. Note that atoms or functional groups that are shared with another Si atom such as the bridging O atom or the methylene group are counted half. Both $Si(CH_2)_{0.5}O_{1.5}$ and $Si(CH_2)O$ are included in the analysis instead of the $Si(CH_2)_xO_{2-x}$ configuration because there is insufficient information in the FTIR spectra to determine the subscript x . We also include an explicit carbon residual in the model to reflect the larger experimental error in the carbon concentration.

The composition information obtained from the RBS and FRES measurements can now be used to derive a mass balance for each of the atomic species in OSG in terms of the number densities of the six bond configurations in the model

$$\sum_{j=1}^6 a_j^k x_i^j = R_i^k \quad i \in (1,4) \quad [A-1]$$

where R_i^k is the fraction of element $k \in \{Si, O, C, H\}$ in film i . x_i^j is the number density of bond configuration j (as numbered in Table A-II) in film i . The coefficients a_j^k represent the contribution of functional group j to element k and are listed in Table A-II. Equation A-1 represents a set of 16 equations in 24 unknowns.

Additional equations can be derived by resorting to the FTIR data. If the infrared absorption cross section for a given vibration mode s of a particular functional group j is the same for all OSG samples, one can write

$$x_{(1+\alpha)}^j / x_1^j = A_{(1+\alpha)}^s / A_1^s \quad \text{for } \alpha \in \{1,2,3\} \quad [A-2]$$

where A_{ij}^s is the integrated area of the absorption band that corresponds to vibration mode s of functional group j for film i . Table A-III lists the seven absorption bands used to construct these equations for the functional groups that can be identified in the FTIR spectra. The situation for the absorption band from 1175 to 990 cm^{-1} , which is associated with Si–O–Si α -stretching, is slightly more complicated because several bond configurations contribute to this band. This band yields three equations of the type

$$\frac{2x_{1+\alpha}^{SiO_2} + (2 - m_{1+\alpha})x_{1+\alpha}^{(CH_3)_{2m}SiO_{2-m}} + 1.5x_{1+\alpha}^{(CH_2)_{0.5}SiO_{1.5}} + x_{1+\alpha}^{(CH_2)SiO} + (2 - p_{1+\alpha})x_{1+\alpha}^{H_{2p}SiO_{2-p}}}{2x_1^{SiO_2} + (2 - m_1)x_1^{(CH_3)_{2m}SiO_{2-m}} + 1.5x_1^{(CH_2)_{0.5}SiO_{1.5}} + x_1^{(CH_2)SiO} + (2 - p_1)x_1^{H_{2p}SiO_{2-p}}} = A_{(1+\alpha)}^s / A_1^s \quad [A-3]$$

Information on the ratio between CH_3 and CH_2 in film i is also obtained from the corresponding asymmetric C–H stretching vibrations in the range from 2968 to 2912 cm^{-1} and the bending modes at 1412 and 1360 cm^{-1} . Eight equations can be added based on the ratios of the corresponding peak areas

$$\frac{0.5x_i^{(CH_2)_{0.5}SiO_{1.5}} + x_i^{(CH_2)SiO}}{2m_i x_i^{(CH_3)_{2m}SiO_{2-m}}} \cdot \frac{2}{3} = A_i^{CH_2} / A_i^{CH_3} \quad [A-4]$$

Altogether the FTIR results yield 29 equations. Thus, together with the mass balances, there are a total of 45 equations in 24 unknowns. This overdetermined system is solved for the number densities of each of the bond configurations using the least-squares method. The results are given in Table V. A χ^2 -statistical analysis of the model constructed here shows that it provides a good fit for the experimental results with a correlation coefficient R^2 of 0.998. In order to assess the applicability of the model to OSG films deposited using different precursors, we have repeated this analysis including OSG coatings deposited using two different precursors⁴⁵ and found the same inverse cross sections within the margin of error.

Table A-III. FTIR absorption bands for each functional group used in the model, vibration mode s in Eq. A-2.

Group	FTIR peaks (cm^{-1})
Si–O–Si	1175–990
Si–CH ₃	1412, 1273, 860–755
Si–CH ₂ –Si	1360
Si–H	2270–2145, 891

References

- M. Morgen, E. T. Ryan, J. H. Zhao, C. Hu, T. H. Cho, and P. S. Ho, *Annu. Rev. Mater. Sci.*, **30**, 645 (2000).
- K. Maex, M. R. Baklanov, D. Shamiryan, F. Iacopi, S. H. Brongersma, and Z. S. Yanovitskaya, *J. Appl. Phys.*, **93**, 8793 (2003).
- N. Hasirci, *J. Appl. Polym. Sci.*, **34**, 2457 (1987).
- A. S. Chawla, *Biomaterials*, **2**, 83 (1981).
- A. S. Chawla, *Artif. Organs*, **3**, 92 (1979).
- A. Grill and V. Patel, *Appl. Phys. Lett.*, **79**, 803 (2001).
- Y. Toivola, J. Thurn, and R. F. Cook, *J. Electrochem. Soc.*, **149**, F9 (2002).
- P. Y. Mabboux and K. K. Gleason, *J. Electrochem. Soc.*, **152**, F7 (2005).
- L. C. Feldman and J. W. Mayer, *Fundamentals of Surface and Thin Film Analysis*, p. 354, North Holland, Elsevier Science Publishing Co., Inc., New York (1986).
- Y. Xiang, X. Chen, and J. J. Vlassak, *J. Mater. Res.*, **20**, 2360 (2005).
- P. J. Mills, P. F. Green, C. J. Palmstrom, J. W. Mayer, and E. J. Kramer, *Appl. Phys. Lett.*, **45**, 957 (1984).
- Y. Xiang, X. Chen, and J. J. Vlassak, *Mater. Res. Soc. Symp. Proc.*, **695**, L4.9 (2003).
- L. R. Doolittle, *Nucl. Instrum. Methods Phys. Res. B*, **9**, 344 (1985).
- L. R. Doolittle, *Nucl. Instrum. Methods Phys. Res. B*, **15**, 227 (1986).
- B. L. Doyle and D. K. Brice, *Nucl. Instrum. Methods Phys. Res. B*, **35**, 301 (1988).
- J. E. E. Baglin, A. J. Kellock, M. A. Crockett, and A. H. Shih, *Nucl. Instrum. Methods Phys. Res. B*, **64**, 469 (1992).
- J. Brus, F. Kolar, V. Machovic, and J. Svitilova, *J. Non-Cryst. Solids*, **289**, 62 (2001).
- C. Rau and W. Kulisch, *Thin Solid Films*, **249**, 28 (1994).
- A. Grill and D. A. Neumayer, *J. Appl. Phys.*, **94**, 6697 (2003).
- Y. H. Kim, M. S. Hwang, H. J. Kim, J. Y. Kim, and Y. Lee, *J. Appl. Phys.*, **90**, 3367 (2001).
- S. C. Deshmukh and E. S. Aydil, *J. Vac. Sci. Technol. A*, **13**, 2355 (1995).
- C. Marcolli and G. Calzaferri, *J. Phys. Chem. B*, **101**, 4925 (1997).
- H. G. P. Lewis, D. J. Edell, and K. K. Gleason, *Chem. Mater.*, **12**, 3488 (2000).
- P. G. Pai, S. S. Chao, Y. Takagi, and G. Lucovsky, *J. Vac. Sci. Technol. A*, **4**, 689 (1986).
- A. L. Smith, *Spectrochim. Acta*, **16**, 87 (1960).
- N. Wright and M. J. Hunter, *J. Am. Chem. Soc.*, **69**, 803 (1947).
- D. V. Tsu, G. Lucovsky, and B. N. Davidson, *Phys. Rev. B*, **40**, 1795 (1989).
- D. D. Burkey and K. K. Gleason, *J. Appl. Phys.*, **93**, 5143 (2003).
- C. C. Chiang, C. C. Chen, L. J. Li, Z. C. Wu, S. M. Jang, and M. S. Liang, *J. Electrochem. Soc.*, **151**, G612 (2004).
- G. Lucovsky, J. Yang, S. S. Chao, J. E. Tyler, and W. Czubatjy, *Phys. Rev. B*, **28**, 3225 (1983).
- P. Bornhauser and G. Calzaferri, *Spectrochim. Acta, Part A*, **46**, 1045 (1990).
- J. Durand, B. Cros, F. Rousseaux, and S. Gujrathi, *J. Mater. Res.*, **7**, 2478 (1992).
- D. K. Basa and F. W. Smith, *Thin Solid Films*, **192**, 121 (1990).
- P. Bornhauser and G. Calzaferri, *J. Phys. Chem.*, **100**, 2035 (1996).
- K. M. McNamara, B. E. Williams, K. K. Gleason, and B. E. Scroggs, *J. Appl. Phys.*, **76**, 2466 (1994).
- C. H. Hsieh, H. Jain, and E. I. Kamitsos, *J. Appl. Phys.*, **80**, 1704 (1996).
- E. Dehan, P. Templeboyer, R. Henda, J. J. Pedroviejo, and E. Scheid, *Thin Solid Films*, **266**, 14 (1995).
- Y. Yamaguchi, Y. M. Xie, S. J. Kim, and H. F. Schaefer, *J. Chem. Phys.*, **105**, 1951 (1996).
- F. Fujimoto, A. Ootuka, K. Komaki, Y. Iwata, I. Yamane, H. Yamashita, Y. Hashimoto, Y. Tawada, K. Nishimura, H. Okamoto, and Y. Hamakawa, *Jpn. J. Appl. Phys., Part 1*, **23**, 810 (1984).
- K. Nakazawa, S. Ueda, M. Kumeda, A. Morimoto, and T. Shimizu, *Jpn. J. Appl. Phys., Part 2*, **21**, L176 (1982).
- M. H. Brodsky, M. Cardona, and J. J. Cuomo, *Phys. Rev. B*, **16**, 3556 (1977).
- H. Shanks, C. J. Fang, L. Ley, M. Cardona, F. J. Demond, and S. Kalbitzer, *Phys. Status Solidi B*, **100**, 43 (1980).
- C. J. Fang, L. Ley, H. R. Shanks, K. J. Gruntz, and M. Cardona, *Phys. Rev. B*, **22**, 6140 (1980).
- Y. Lin and J. J. Vlassak, *In preparation*.